ARTICLE

Understanding Why Poly(Acrylic Acid) Works: Decarbonylation and Cross-Linking Provide an Ionically Conductive Passivation Layer in Silicon Anodes

Trevor R. Martin[a], Ryan T. Pekarek[a], Jaclyn E. Coyle[a], Maxwell C. Schulze[a], Nathan R. Neale[a]*

Poly(acrylic acid) (PAA) is commonly used as a binder for fabricating silicon (Si) anode active materials in lithium-ion batteries due to its useful properties including high polar solvent solubility, good rheology, and strong adhesive properties. However, the role and evolution of PAA during electrode fabrication, cycling, and calendar aging are not well understood. In this work, we reveal the evolution of PAA during electrode curing and relate its chemical change to the final electrode properties and performance. These studies are made possible using two types of in situ attenuated total reflectance-infrared Fourier transform (ATR-FTIR) spectroscopy: thermal ATR-FTIR to probe the cross-linking reaction, and ATR-FTIR spectroelectrochemistry of three-dimensional composite electrodes, a unique technique developed herein that probes the solvation dynamics of lithium ions at the silicon anode interface under electrochemical polarization. Specifically, we show that PAA undergoes a thermally-mediated, cross-linking decarbonylation reaction to form an ether-based network polymer. To show the importance of the polyether moieties, we synthesize partially esterified PAA analogues that do not undergo this cross-linking decarbonylation reaction and we correlate the degree of cross-linking to half-cell performance metrics. Finally, we unveil the mechanism of the polyether binder performance through in situ FTIR spectroelectrochemistry and show that PAA acts as an interfacial material that conducts lithium-ions, limits solvent molecule access to the Si surface, and stabilizes the electrode against parasitic lithium inventory loss at high state of charge for an extended period of time.

Introduction

Poly(acrylic acid) (PAA) based binders are ubiquitous in composite electrodes in lithium-ion batteries (LIB). High silicon (Si) content LIB anodes have received considerable interest recently as a promising technology to significantly boost LIB energy densities.[1,2] However, Si suffers from a number of detrimental properties including an exceptionally large volume change during lithiation and the presence of unstable surface species.[1] Several reports have examined how various polymeric binders (including PAA and others) impact the mechanical stability and cycling performance of silicon anodes.[3–7] Other work has shown that binder chemistry also plays an important role in dictating slurry properties,[8,9] final electrode morphology,[10,11] and the overall performance of Si anodes.[12,13] In addition, significant advances have been made in device performance by implementing new structural variations of PAA and other carboxyl-containing polymers.[14–17] Other investigations have taken this concept one step further by tailoring Si nanoparticle (NP) surface chemistry to covalently link polymeric binders to the Si NP surface.[18,19] Given this body of literature, it is now well-understood that binders can experience a variety of chemical and structural evolutions during slurry processing and electrode curing that can influence the interfacial chemistries that lead to the solid electrolyte interphase (SEI).

Despite these significant improvements in electrochemical performance, the dynamic nature of interfacial binder chemistry for composite Si anodes remains incompletely understood. For example, the various roles binders play as conformal layers that coat silicon nanoparticles,[10] that react with electrolyte molecules,[20,21] impact SEI formation,[13,22] and influence ionic conductivities,[14] have all made decoupling these interrelated effects particularly challenging for Si anodes.[23–28] This work aims to build on previous efforts to further elucidate the role and evolution of PAA interfacial coatings during electrode fabrication, cycling, and long-term voltage holds. We introduce systematic variations in the chemical structure of PAA and examine how this binder chemistry impacts the evolution of the electrode cycling behavior, calendar-life performance, and interfacial properties of Si anodes by two different in situ attenuated total reflectance-Fourier transform infrared (ATR-FTIR) spectroscopy methods. Our results suggest that the polymeric binder is more than a glue that holds the composite anodes together and plays a critical role in dictating cell performance and interfacial chemistry.

a. Chemistry and Nanoscience Center, National Renewable Energy Laboratory, Golden, CO, 80401, USA. E-mail: nathan.neale@nrel.gov

Results and Discussion

In Situ Spectroscopy of Binder Thermal Curing

Poly(carboxylic acids) are known to undergo cross-linking reactions between adjacent carboxylic acids to form anhydrides, which are used as intermediates in paper and textile making to cross-link cellulose fibers. Cross-linking occurs via reactions of the anhydride intermediates with cellulose hydroxyls to give cellulosic esters that provide structural integrity to the paper or textile.[29–31] When considering the behavior of the poly(carboxylic acid) PAA in a Si NP battery anode, we questioned whether reactions between PAA anhydride intermediates and surface silanols on Si active materials also form esters, but in this case silyl esters, that improve mechanical stability of Si-PAA anodes. Conversely, we wondered whether these species might be a source of instability in Si-PAA electrodes given our finding that silyl esters are chemically unstable in a conventional LiPF$_6$-carbonate battery electrolyte.[23]

To test these hypotheses, we developed a simple method to vary the molecular structure PAA by deactivating some carboxyl moieties within the PAA backbone through esterification with pentanol as illustrated in Scheme 1. We hypothesized that this method affords a simple way to systematically decrease the proportion of acid moieties that would otherwise undergo cross-linking reactions with other acid groups in the PAA chain and the Si surface (via silanols). Here, we focus on three polymers: 0% esterified PAA (unmodified), 25% esterified PAA (E-PAA), and 50% E-PAA, where the approximate m:n ratios shown in Scheme 1 are 0:4, 1:3, and 2:2, respectively. It is important to note that this reaction proceeds via a reversible condensation reaction mechanism, which occurs in equilibrium with the associated hydrolysis reaction and is dependent on the relative concentrations of water, pentanol, and PAA. We chose to use pentanol due to its aliphatic nature (relatively chemically inert) and appropriate boiling point (above water at 138 °C), where increasing alkane length (beyond pentyl) leads to higher boiling points but poor polymer solubility due to decreased macromolecular polarity. To synthesize these E-PAA materials, pentanol is added to PAA solutions in water, thereby forming some amount of E-PAA in equilibrium. As the solution is heated and dried under vacuum, the equilibrium point shifts as water is evaporated more rapidly than pentanol. Once the polymer is dried, the final product has a level of esterification proportional to the starting pentanol stoichiometry.

We first studied whether deactivating PAA to cross-linking results in weaker mechanical interactions with Si. To quantify the adhesion of these polymers to a Si surface, we employed a cantilever beam test (CBT) method that was originally devised
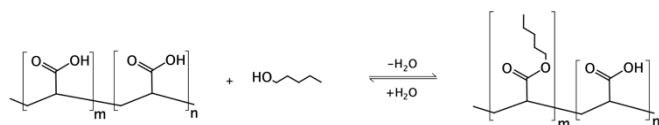
Scheme 1. Synthetic modification of binder where a portion of the PAA carboxyl moieties react with pentanol to form esterified PAA (E-PAA) via a simple condensation reaction.

as a tool to determine the strength of encapsulant adhesion in a silicon photovoltaic module.[32,33] The CBT data analysis methods (Figure S1) and apparatus (Figure S2) are also discussed in detail in the supporting information. We implemented a variation of this method to quantify the strength of adhesion between the three polymers and a native oxide-terminated Si wafer. The normalized debond energy data corroborate our hypothesis that deactivating -COOH units in the binder affect Si/PAA interaction and show that there is a systematic decrease in the strength of adhesion to the Si surface as the degree of PAA esterification increases (Figure S3).

Next, we used in situ ATR-FTIR to probe the second part of our hypothesis that increasing esterification should lead to less self-reaction between carboxylic acid groups in the PAA polymer chain. Specifically, in situ FTIR spectroscopic data were continuously collected during thermal drying and curing under vacuum, thereby studying the evolutions in conformation and chemical structure that occur during a typical electrode fabrication process. In the first set of experiments, FTIR spectra were collected as aqueous polymer solutions using a temperature ramp from ambient to 100 °C under vacuum (Figures 1a, 1c, and 1e). In the second set of experiments, the resulting polymer films were held at 100 °C under vacuum for 24 h (Figures 1b, 1d, and 1f). Each pair of experiments was conducted with PAA, E-PAA (25%), and E-PAA (50%) for a total of six data sets. Details of the experimental apparatus are shown in Supporting Information Figure S4.

The difference spectra from the temperature ramp experiment mimicking film drying (Figures 1a, 1c, and 1e) all exhibit relatively similar sets of peaks that are consistent with the PAA and E-PAA structures shown in Scheme 1, where vibrations assignable to ν C=O acid stretch (1700–1800 cm^{-1}), δ C–O–H acid bend (1350–1400 cm^{-1}), and ν C(O)–O acid stretch (1200–1250 cm^{-1}) are present. In contrast, the difference spectra from the temperature hold experiment emulating film curing (Figures 1b, 1d, and 1f) are dramatically different. A detailed analysis of these data indicates several important trends. First, all of the spectra in the temperature ramp experiments show an increase in the C=O and C–O stretching regions associated with concentration of the polymer solution and film deposition on the ATR crystal. Second, as the polymer film dries, we identify two different solid-state conformations, the gauche (1757 cm^{-1}) and trans (1698 cm^{-1}) polymer forms, previously assigned by Park and colleagues.[34] Third, the temperature hold experiments reveal that major structural and chemical changes occur between polymer units during electrode drying. Whereas both the PAA and E-PAA (25%) polymers exhibit very significant changes (Figures 1b and 1d), the E-PAA (50%) polymer is relatively invariant based on only minor changes in the difference spectra over the 24-h temperature hold (Figure 1f). Delving into the PAA and E-PAA (25%) difference spectra in more detail reveals that these polymers undergo losses of peaks associated with the gauche carboxylic acid structure (gauche C=O carbonyl, C–O–H bend, and C(O)–O stretch; Figures 1b and 1d). In addition, a new peak associated with a n C–O ether stretch (~1050 cm^{-1}) appears in all spectra and is especially prevalent for the PAA and E-PAA
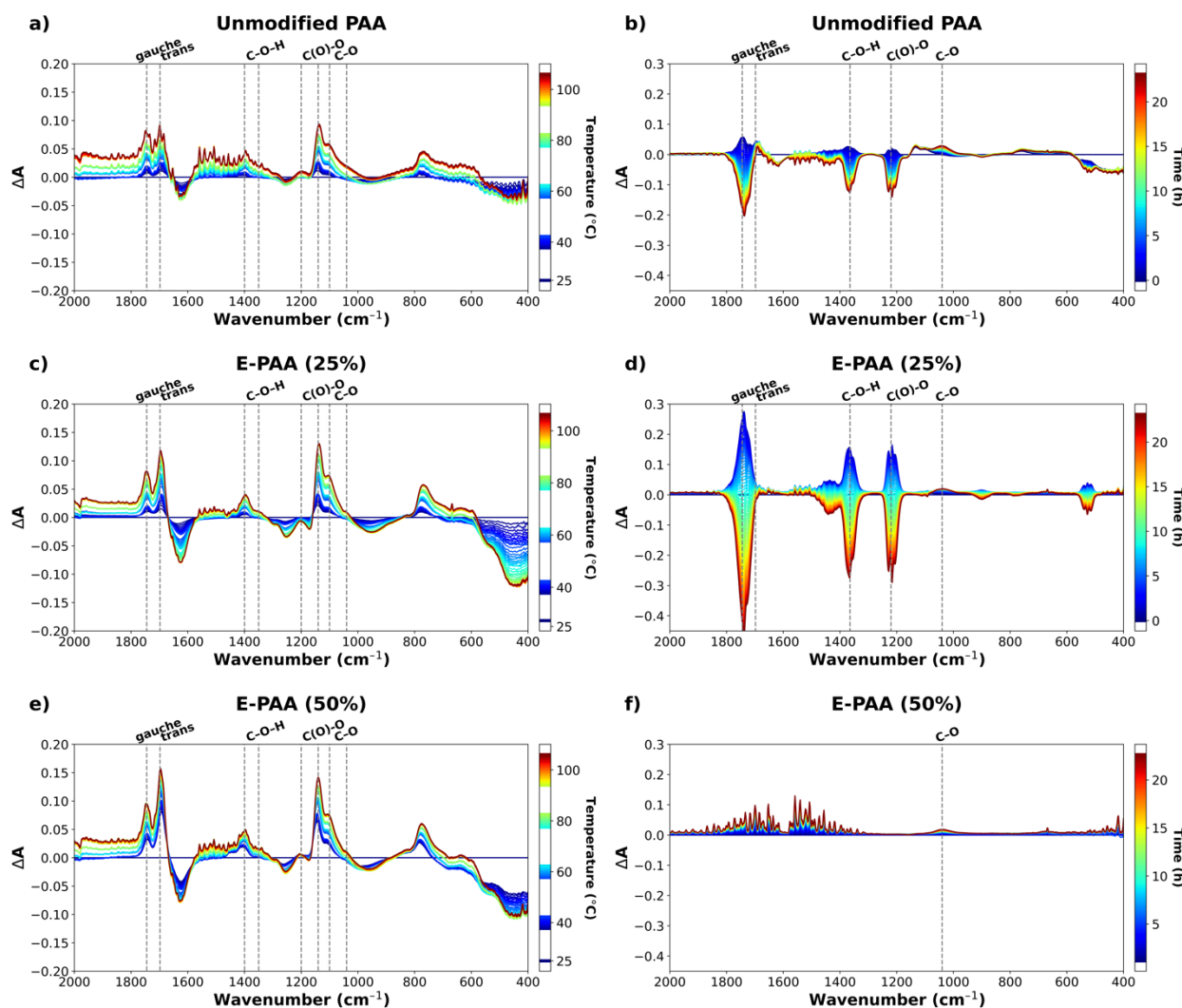
Figure 1. In situ ATR-FTIR spectroscopy of binder drying: Variable temperature spectra during temperature increase from room temperature to 100 °C (a, c, e). Spectra collected at 100 °C during 24 h curing experiment (b,d,f). Three polymers are shown: unmodified PAA (a, b); 25% esterified PAA (c, d); 50% esterified PAA (e, f). All spectra are difference spectra, and unsubtracted spectra are shown in Figure S5.

(25%) samples consistent with the degree of condensation expected from available carboxylic acid moieties in these three samples (see Figure S6 for a detailed comparison of the evolution of the C–O region). The degree of pre-esterification with pentanol also directly impacts the relative ratios of the gauche and trans isomer peaks and, therefore, the polymer tacticity (see Supporting Information for full discussion). Furthermore, these changes in polymer conformation also provide evidence supporting the relative m to n stoichiometries (degree of esterification) of the polymers as presented in Scheme 1.

These results provide strong evidence that vacuum drying of PAA and E-PAA binders causes a decarbonylation reaction between unesterified adjacent carboxylic acid moieties as depicted in Scheme 2. Importantly, the spectra do not exhibit evidence of polyanhydride formation through a condensation reaction, which would give rise to high energy C=O vibrations at >1800 cm^{-1}. Since none are observed (Figure S5 and zoomed region shown in S7), we theorize that polyanhydrides may exist as a minor species or as unobserved intermediates, which

ultimately forms a polyether structure through subsequent decarbonylation as depicted in Scheme 2. Previous works have shown that PAA undergoes cross-linking reactions via polyanhydride formation within the temperature range of 100 to 200 °C.[20,34] It was also suggested that subsequent
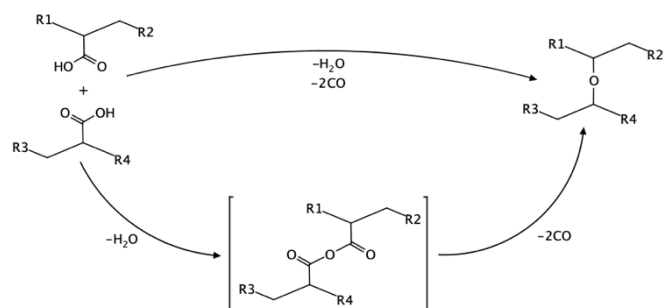
Scheme 2. Proposed decarbonylation reaction between carboxyl moieties to form the final cross-linked polyether network either directly or a stepwise condensation reaction, forming an unobserved cross-linked polyanhydride, and subsequent decarbonylation to the polyether.

decarbonylation could occur, though ethers were not observed.[34] Here, we definitively observe cross-linked polyether moieties for the first time, to our knowledge, from decarbonylation of PAA. We hypothesize the reason this is observed in our experiment and not prior works is our use of vacuum (roughing pump pressure ~10^{-2} Torr), which likely shifts any equilibrium between carboxylic acid, anhydride, and ether toward the ether. To further confirm the formation of polyether moieties, we performed an analogous ex situ experiment where a PAA film was heated to 100 °C for 24 h under vacuum, analyzed using ATR-FTIR, reheated at 150 °C for 3 h under vacuum, and reanalyzed using ATR-FTIR. Figure S8 shows a strong polyether signal after the 100 °C step and a subsequent signal increase after the 150 °C step, thereby corroborating our in situ data and demonstrating that this polyether formation occurs (and is more pronounced) during typical electrode processing conditions.

Finally, we note that 150 °C is a common vacuum drying temperature for Si-PAA anodes[9] and is significantly higher than our experimental conditions (100 °C, limited by the heated ATR-FTIR stage). Assuming a simple first-order rate law obeying the Arrhenius equation, for each 10 °C temperature rise, a doubling of the reaction rate is expected. Therefore, we suggest that our experiment conducted at 100 °C for 24 h closely approximates the chemical reactions that occur under more typical 150 °C electrode drying conditions.

Electrochemical Analysis of Composite Electrodes

To test the impact of these chemical and structural binder variations on silicon anode electrochemistry, we fabricated a set of model composite electrodes using the three polymeric binders in composite Si anodes with 80% Paraclete Si NPs (~150 nm average diameter), 10% PAA or E-PAA, and 10% Timcal C65 conductive carbon in a half-cell configuration with a lithium metal counter electrode. Figure 2 shows the specific capacity of the electrodes during delithiation. For each set of cells, the first three formation cycles were performed at a rate of C/20 while each subsequent cycle was performed at a rate of C/5. Each binder formulation was used to produce at least three cells, where the data presented are the mean of the cycling data with error bars representing one standard deviation in specific capacity. The variations in capacity can be attributed to inhomogeneities in the electrode films and to changes in the areal loading of the electrodes between cells. It is important to emphasize that these electrodes were fabricated to elucidate the role and influence of the variations in binder structure as model high-Si-content electrodes and are not optimized, high-performance Si anodes. Furthermore, the slurries used to fabricate these cells were principally optimized to fabricate effective in situ ATR-FTIR spectroelectrochemical cells. Accordingly, all the electrodes show a significant decay in reversible capacity after approximately 20 cycles and a significant variation in early cycle performance depending on electrode loading. However, the data in Figure 2 are presented here to help elucidate an important trend, where the average percent loss in reversible capacity per cycle is correlated with the degree of esterification, as highlighted in Figure 2c.

The data shown in Figure 2 indicate that as the degree of esterification increases, the less rapid the mean capacity fade per cycle. We hypothesize that this observation is directly related to the degree of cross-linking present in the binders. Specifically, as more carboxyl moieties are deactivated via esterification, fewer polyether moieties are formed, and the polymers are less cross-linked. Given the well-established knowledge that less cross-linked polymers remain more flexible and mechanically resilient, we surmise that increasing esterification leads to a more compliant binder that can better withstand the Si volume expansion-contraction that occurs during lithiation and delithiation. These subtle changes in mechanical properties are manifested as a slightly slower rate of capacity fade (Figure 2c), where continued cycling of these large ~150 nm diameter Si particles presumably leads to their mechanical fracture and electrical isolation of some portion of the Si, which is mitigated by the more compliant esterified E-PAA cf. PAA. In support of this conclusion, it has previously been demonstrated that changing binders can impact the mechanical properties of the composite, where accommodating volumetric strain during lithiation and minimizing subsequent cracking are critical to improving electrode performance.[35] To further
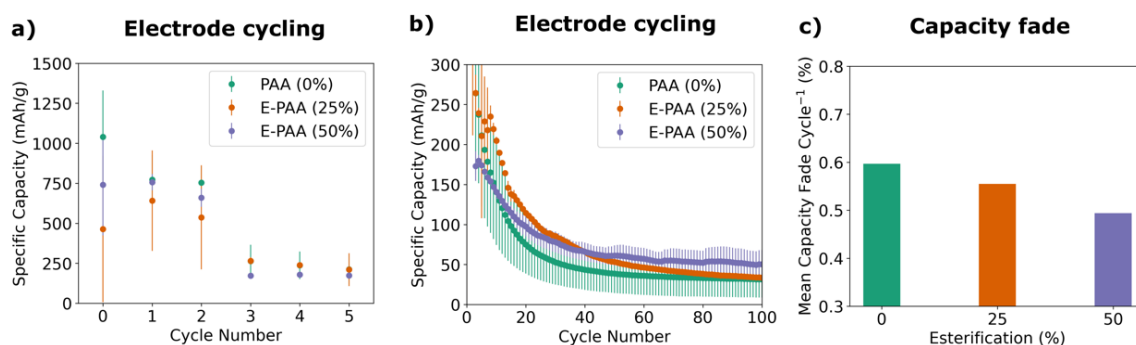

Figure 2. a) Specific capacity of the electrodes for the first 5 cycles, where the first 3 cycles are the C/20 formation cycles. b) Specific capacity comparison of the electrodes for 100 cycles. Data are normalized relative to electrode mass and are presented as mean values with error bars representing one standard deviation. c) Mean capacity fade of the electrodes after the first 3 formation cycles expressed as a percent reduction in capacity between subsequent cycles relative to the degree of binder esterification.

validate this hypothesis, we also conducted a series of nanoindentation tests on pristine Si composite anodes (Figure S9). These data support this conclusion, since as the degree of esterification increases there is a small decrease in the elastic modulus of the composite films.

To understand how the degree of esterification also impacts the potential long-term performance of Si anodes, we also conducted a voltage-hold test using an analogous set of coin cells assembled in a half-cell configuration. This test is designed to mimic the open circuit voltage (OCV) holds of a long-term calendar-life test under accelerated conditions.[36,37] A set of analogous electrodes were fabricated using the three different binders and the cells were cycled three times at a rate of C/20 and then held at a potential of 100 mV for 180 h. The voltage-hold data are presented in Figure 3. In contrast to the cycle lifetime data in Figure 2, the data shown in Figure 3 exhibit an important trend where the parasitic current increases with the degree of esterification. We theorize that this effect also is related to the degree of cross-linking, but unlike under cycling where less cross-linking is beneficial to the mechanical properties, we suspect that under constant polarization, a less cross-linked electrode could allow for greater diffusion of electrolyte species to the Si surface, where they become irreversibly reduced (i.e., undergo parasitic reactions). This theory is also in agreement with previous work, where it has been demonstrated that binders with a stronger bond to the Si surface are correlated to improved cell cycling performance.[3]
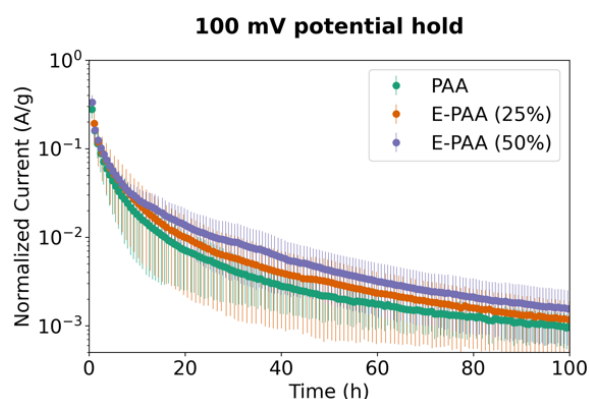

Figure 3. Residual current of electrodes during 100 mV vs Li/Li$^+$ voltage hold. Data are normalized relative to electrode mass and are presented as mean values with error bars representing one standard deviation.

In Situ Spectroelectrochemical Analysis

To further probe this relationship and examine the electrolyte permeability hypothesis in detail, we developed a unique in situ ATR-FTIR spectroelectrochemical method to study how electrolyte solvent dynamics evolve during initial electrode wetting and open circuit voltage (OCV) holds. Due to the high level of complexity inherent in this technique and to maximize the difference between the degree of esterification, we fabricated composite electrodes using the unmodified PAA and E-PAA (50%) binders and Gen2 electrolyte (1.2 M LiPF$_6$ in 3:7 ratio by mass of ethylene-carbonate (EC) to ethyl-methyl-carbonate (EMC)). Composite electrodes are deposited onto

copper mesh current collectors similar to the technique used for in situ surface-enhanced Raman experiments reported recently.[24] Here, a half-cell battery is constructed directly onto a chemically robust diamond ATR crystal, which enables investigation of this composite electrode on copper mesh.

Figure 4 illustrates how the ATR-FTIR spectra evolve during an 8-h OCV hold to emulate the wetting process in a freshly assembled battery for two representative electrodes. For the E-PAA (50%) sample (Figure 4b), all of the prominent electrolyte peaks increase relatively uniformly over time (note: all peak assignments from our previous study in ref. 23). This indicates that the electrolyte diffuses into the electrode and that the polymeric binder operates as an electrolyte-conducting medium. In stark contrast, the PAA sample (Figure 4a) exhibits a significantly different trend, where the P–F stretching mode absorbance at approximately 840 cm^{-1} from the PF$_6^-$ ion increases significantly during the OCV hold. A simple charge neutrality argument suggests that the PF$_6^-$ results from Li$^+$ being pulled into the electrode film. Moreover, the free (Li-uncoordinated) EMC C=O stretching absorbance at approximately 1744 cm^{-1} decreases over time with a concurrent increase in peak intensity from Li-coordinated carbonates Li-EC (1763 cm^{-1}) and Li-EMC (1716 cm^{-1}). The PAA spectra also exhibit a similar trend in the 1265 cm^{-1} C(O)–O ester region where the free (Li-uncoordinated) EMC peak decreases over time with a concurrent increase in nearby Li-coordinated peaks resulting from Li-EMC (1306 cm^{-1}) and Li-EC (1195 cm^{-1}). Thus, it appears that Li$^+$ infiltrates the PAA film without significant
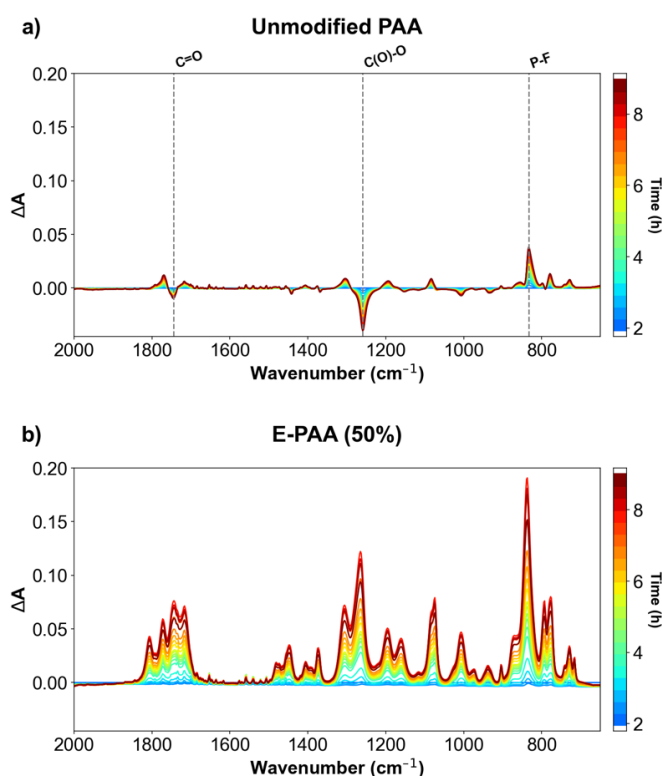

Figure 4. Infrared difference spectra during initial OCV hold for composite silicon nanoparticle electrodes using an unmodified PAA binder a) or an E-PAA (50%) binder b). All spectra are difference spectra, and unsubtracted spectra are shown in Figure 10.
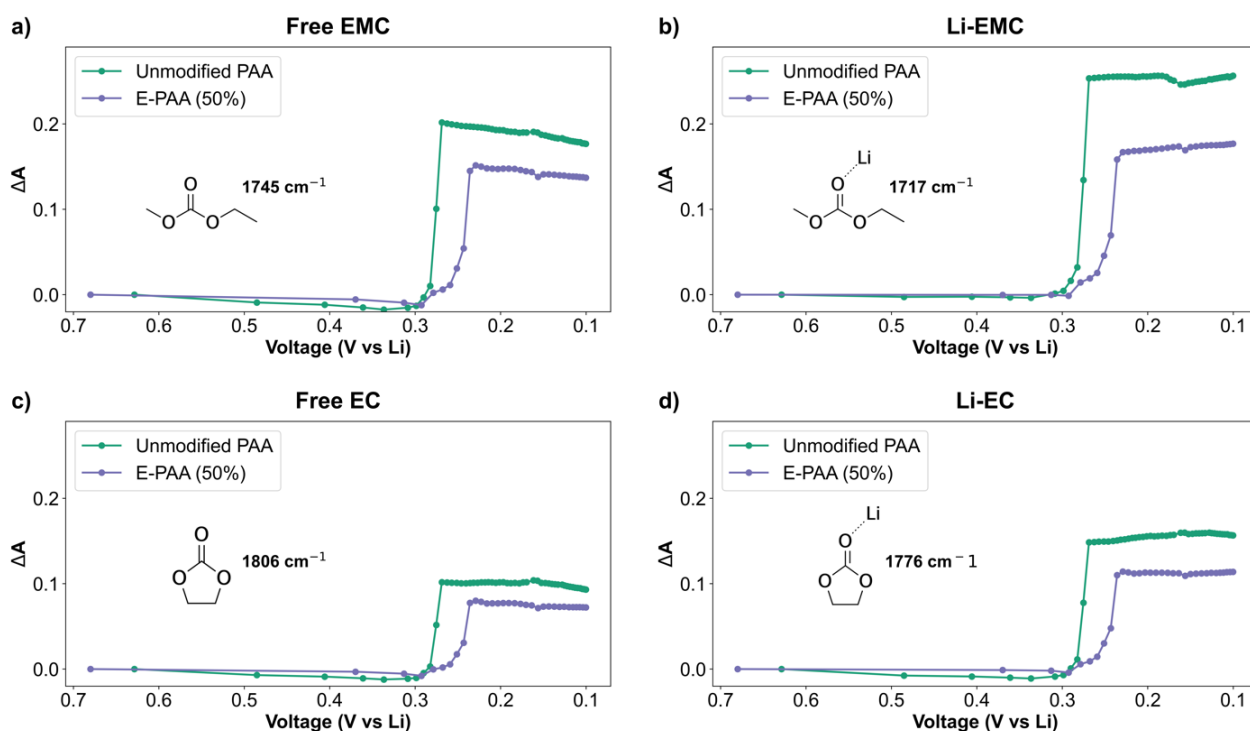
Figure 5. Peak intensity evolution of ATR-FTIR difference spectra during lithiation for composite silicon nanoparticle electrodes using an E-PAA (50%) binder or an unmodified PAA binder. (a) Free (Li-uncoordinated) peak evolution for EMC during lithiation. (b) Li-coordinated peak evolution for Li-EMC during lithiation. (c) Free (Li-uncoordinated) peak evolution for EC during lithiation. (d) Li-coordinated peak evolution for Li-EMC during lithiation. Unsubtracted spectra are shown in Figure S11.

accompanying coordinating carbonate solvent. These results indicate that the cross-linked polyethers in the PAA binder serve as a selective membrane for Li-ions and exclude free carbonate solvent molecules, whereas the less cross-linked E-PAA binder facilitates the rapid swelling of all electrolyte species.

Electrochemically cycling these composite electrodes provides complementary and reinforcing information about the electrolyte permeation behavior of PAA versus E-PAA. Tracking the peak maximum for individual species reveals how its concentration changes as a function of potential. The data presented in Figure 5 show the relative changes in free (Li-uncoordinated) and Li-coordinated EC and EMC solvent molecules as they infiltrate the two composite electrodes, with all difference spectra relative to the baseline spectrum following the 8-h OCV hold. Complete in situ ATR-FTIR absorbance difference spectra as a function of applied potential (from ~0.7 to 0.1 vs Li/Li+) are provided in Figure S11. First, we observe that the absorbance intensity from all four carbonate species in the PAA sample (green traces in Figure 5a, 5b, 5c, and 5d) increase earlier in the lithiation cycle (at a more positive during the final stages of lithiation compared with those species in the E-PAA sample. We hypothesize that this trend is a result of the fact that the E-PAA electrode has already swelled with more electrolyte than the PAA sample following the 8-h OCV hold (the baseline at $\Delta A = 0$). Therefore, the PAA film undergoes a stronger polarization-induced electrolyte swelling than the E-PAA electrode since the PAA film is not effectively wetted during the OCV hold (see Fig. 4a). Second, the difference in the plateau ΔA levels for the Li-coordinated species (Figure 5b and

5d) is higher compared with the free solvent species (Figure 5a and 5c). In particular, the uptake of Li-coordinated Li-EMC is more pronounced for the PAA electrode and is more significant than the uptake of the three other species (ΔA ~0.25 cf. 0.1–0.2 for EMC, EC, and Li-EC). This observation is substantiated by other studies that have shown that the addition of EMC is critical for increasing diffusion coefficients.[38] In related work, Borodin and coworkers showed that linear carbonates such as dimethylcarbonate can bind to Li+ in a bidentate fashion, whereas bindentate binding from cyclic carbonates (EC) is much weaker.[39] This suggests that, despite the stronger binding affinity to Li+ from EC than EMC in bulk solution,[23] Li-ions achieve a higher degree of solvation by desolvating EC and remaining coordinated to EMC when passing through a polyether-based SEI.

Poly(ethylene oxide) (PEO) films are commonly used as lithium ion conducting materials, and PEO-like oligomers that facilitate lithium-ion conductivity have been previously identified by our group as an important target for optimizing Si anode interfacial chemistry and device performance.[18,40] Accordingly, a PAA-based composite electrode appears to enhance the ability for "carbonate-solvent lean" Li-ion diffusion, limiting the amount of carbonate solvent molecules (here, primarily EC and to a lesser degree, EMC) that are able to access the electrode surface. Consequently, a lower overall residual current resulting from decreased carbonate solvent reduction is observed at the anode. This ultimate consequence – lower residual current in films with a greater degree of cross-
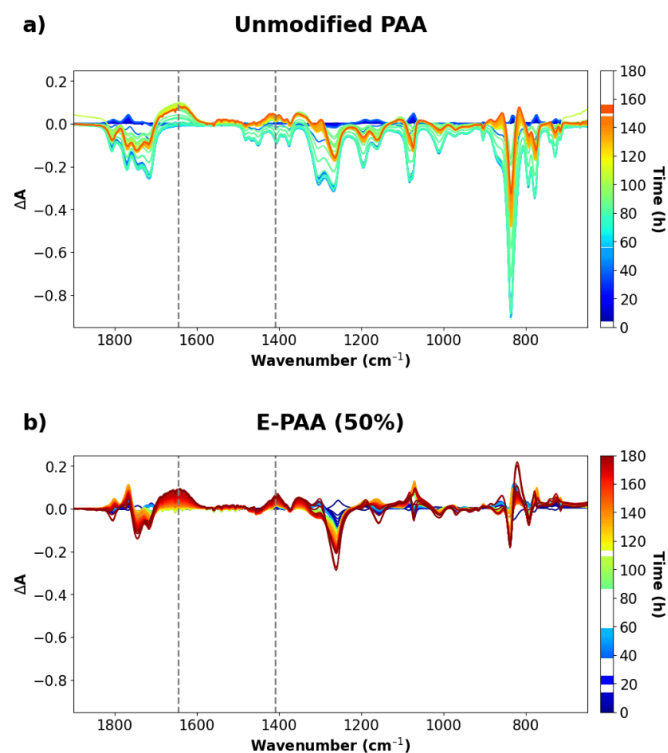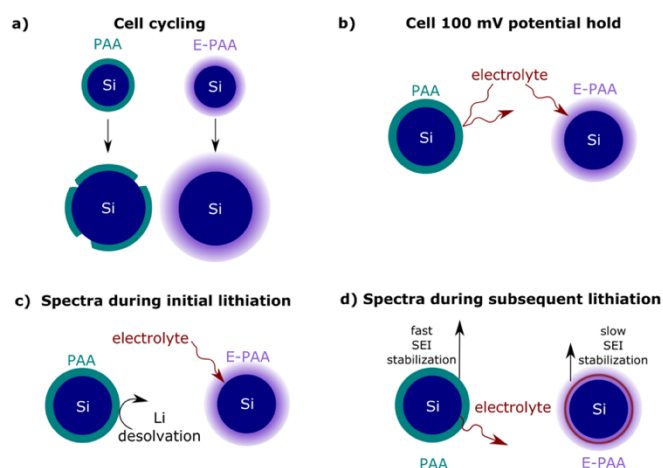
a)

Unmodified PAA

b)

E-PAA (50%)

Figure 6. Infrared difference spectra during 160–180 h 100 mV potential hold (vs. Li/Li⁺) for a) PAA and b) E-PAA (50%) based composite silicon nanoparticle electrodes. New Li-carboxylate-like species appear in the 1650-1600 cm⁻¹ and 1450-1400 cm⁻¹ regions, which are highlighted for reference. Full spectra are shown in Figure S12.

a) **Cell cycling**

b) **Cell 100 mV potential hold**

c) **Spectra during initial lithiation**

d) **Spectra during subsequent lithiation**

Scheme 3. Representations and summaries of the interfacial evolutions that occur during electrochemical testing and in situ spectroelectrochemical testing: (a) The E-PAA (50%) interface is more resistant to mechanical failure during cell cycling when compared to the cross-linked polyether PAA interface. (b) The E-PAA (50%) interface promotes electrolyte diffusion to the silicon surface, while the polyether PAA interface blocks electrolyte diffusion to the silicon surface. (c) During initial lithiation and OCV holds, the in situ ATR-FTIR spectra show that the E-PAA (50%) interface uptakes all solvent species, whereas the polyether PAA interface promotes Li-ion desolvation. (d) During subsequent lithiation, the in situ spectra show that the E-PAA (50%) interface infiltrates solvent species more readily and forms an SEI layer more slowly than the polyether PAA interface, which expels solvent species and forms a more passivating SEI.

linked polyether moieties – is exactly what is observed from our calendar lifetime voltage hold experiment (Figure 3).

Lastly, we investigated how these results help explain the differences in parasitic current shown in Figure 3 and discussed previously. These cells were then cycled at a rate of C/20 three times and subsequently held at 100 mV (relative to Li/Li⁺) for between 160 and 180 h. Figure 6 shows the evolution in the difference spectra during the voltage hold for both the PAA and E-PAA electrodes. Figure 6a shows that in the case of PAA, there is a significant loss of all prominent electrolyte peaks after approximately 60 h of voltage hold. In comparison, the changes in the E-PAA (50%) spectra are less pronounced and occur primarily at a later time during the voltage hold (Figure 6b). We hypothesize that this effect is related to the previous observations, where the PAA-based coatings are more likely to facilitate Li-ion desolvation schemes at the SEI/electrolyte interface, do not swell with as much electrolyte as E-PAA during initial voltage holds, and uptake electrolyte molecules earlier in lithiation at less reducing potentials. Accordingly, these data show that once an equilibrium point is reached and the Si NPs are effectively lithiated, the PAA interfacial coatings comparison to the E-PAA interfacial coatings. Furthermore, both sets of spectra show evidence of the formation of broad (not molecular) Li-alkylcarbonate species as evidenced by the subsequently expel electrolyte molecules more readily in in comparison to the E- PAA interfacial coatings. Furthermore, both sets of spectra show evidence of the formation of broad (not molecular) Li-alkylcarbonate species as evidenced by the

asymmetric (1650–1600 cm⁻¹) and symmetric (1450–1400 cm⁻¹) carbonate stretching vibrations (dashed black verticle lines, Figure 6), comparable to those for the putative SEI component lithium ethyeledicarbonate (LiEDC).[41] These new peaks appear earlier in the PAA-based composite film and can be associated with the formation of an SEI containing lithium alkylcarbonate species. We hypothesize that these peaks are further evidence that the PAA-based interfacial coatings more readily expel electrolyte molecules and more rapidly form a less reactive SEI layer in comparison to the E-PAA-based electrodes.

Finally, we summarize these findings in Scheme 3 and present them within the context of our initial half-cell electrochemical and binder curing results. Scheme 3a illustrates how the effectively non-cross-linked E-PAA-based electrodes are more resilient to volumetric strain during cell cycling, which results in slight improvements in cell cycling performance. Conversely, Scheme 3b depicts how the E-PAA-based electrodes provide pathways for electrolyte molecules to react with the Si surface, which results in a higher parasitic current during extended voltage holds. Scheme 3c shows how the E-PAA-based electrodes will swell with electrolyte species at the interface, whereas the PAA-based films facilitate changes in Li coordination at the interface. Scheme 3d illustrates how the PAA-based films promote the rejection of electrolyte solvent molecules and the more rapid formation of a passivating SEI in comparison to the E-PAA-based electrodes. These results can be used to help inform future research areas, where optimizations in binder structures can be used to boost cycling performance

but must also promote interfacial stability, ionic conductivity, and effective changes in lithium-ion coordination schemes. The importance of the numerous impacts that electrode binders have on all aspects of electrode fabrication and cell performance must be addressed to optimize an electrode that retains long-term performance and that minimizes parasitic reactions and self-discharge.

Conclusions

We showed a new polymeric binder reaction scheme where the carboxyl moieties in PAA undergo decarbonylation to form cross-linked polyether structures in silicon nanoparticle composite anodes during electrode curing. We demonstrated that the binder chemical and structural evolution directly relates to the cycling performance and the long-term parasitic current levels of Si electrodes. Furthermore, we developed a novel in situ electrochemical ATR-FTIR spectroelectrochemical technique that reveals how these variations in binder chemical structure influence the Li-ion solvation dynamics at the electrode interface. Finally, we used these data to propose that the polyether structures formed after PAA binder curing are critical for facilitating efficient Li-ion desolvation reactions, effective Li-ion conduction modes, and stable SEI layers at the silicon anode interface.

Experimental Methods

Poly(acrylic acid) Modification

All precursors were acquired from Sigma-Aldrich and used as received unless otherwise noted. Esterified PAA (E-PAA) samples were prepared by adding 38 µL or 76 µL pentanol (E-PAA (25%) or E-PAA (50%) respectively) to 100 mg of 450k MW PAA dissolved in 5 mL deionized water. The solutions were stirred at 300 rpm and heated to 50 °C for 60 minutes.

Electrode Preparation

Electrodes were prepared by combining 2.0 mL of the PAA and modified E-PAA solutions (containing 40 mg polymer) with 320 mg G18 Paraclete silicon nanoparticles, and 40 mg of Timcal C65 conductive carbon in a nominal mass ratio of 80% silicon, 10% binder, and 10% conductive carbon. The slurries were stirred at ambient temperature until visibly homogenous (approximately 1 h). Each slurry was then mixed for 90 s using a planetary mixer (Mazerustar KK-250S planetary mixer) before being cast onto a Cu foil using an MTI corporation compact blade casting coater with a wet gap of 250 µm and a casting speed of ~1 cm/s. The electrodes were subsequently cured under vacuum at 150 ºC for 24 h.

Half-cell Fabrication and Electrochemical Testing

The electrodes were tested using 2032 coin cells in the half-cell configuration. Each electrode was tested in multiple times, using between 3 and 5 identical cells with 14 mm-diameter circular punches from each electrode. The half-cells were assembled in a glovebox with the 14 mm silicon electrodes as

the positive electrode. The negative electrodes used were 9/16 inch diameter circular punches of Li metal foil (Alfa Aesar 10769, 0.75 mm thick, 99.9% metals basis) that were cleaned with a toothbrush before being pressed onto a 15 mm-diameter, 1 mm-thick, and stainless-steel spacer with a stainless-steel wave spring positioned on the opposite side. The electrodes were separated by a 19 mm circular punch of porous polypropylene separator (Celgard 2325). Each cell was injected with 20 µL of the GenF electrolyte ($LiPF_6$ in fluoro-ethylene-carbonate/ethylene-carbonate/ethyl-methyl-carbonate 1:2.7:6.3 by mass) onto each side of the separator (40 µL total) before the cells were sealed by a hydraulic crimper. Each cell was allowed to rest at open circuit potential for 4 h before being galvanostatically cycled between 0.1 V and 1.5 V vs Li at C/20 forming cycles followed by cycling at C/5.

Thermal In situ Infrared Spectroscopy

Experiments were performed using a Bruker Alpha FTIR spectrometer affixed with a temperature-controlled diamond ATR module. All spectra were collected using a 100 scans and 4 cm^{-1} resolution. An aqueous modified or unmodified PAA solution (1 mL) was dropped onto the diamond ATR element and covered with a custom-built PEEK housing with a vacuum port (diagram shown in supporting information Figure S4). The vacuum port was then connected to a Schlenk line. A background spectrum was collected at 25 °C under atmospheric pressure, the cell was then evacuated. Two complementary experiments were performed: a temperature ramp experiment and 100 °C hold over 24 h. In the former, a spectrum was collected at 25 °C then the stage was heated to 40 °C for 10 spectra (~10 min). The procedure was repeated for 60, 80, and 100 °C, except the 25 spectra (~30 min) were collected at the final temperature. In the second experiment, temperature was increased directly to 100 °C. Spectra were collected every 20 min over 24 h.

Infrared Spectroelectrochemistry

Spectroelectrochemical experiments were collected on a ThermoFisher Nicolett 7600 using a liquid nitrogen cooled MCT-A detector and a Smart iTx diamond ATR attachment. A custom PEEK electrochemical cell was constructed and used to perform the experiment. A diagram of the experiment is shown in the supporting information Figure S13. The ATR plate was protected and made conductive using Kapton tape and copper foil with a small hole cut for the diamond ATR element. In order to minimize unwanted electrochemical reactions on the copper surface (opposed to the intended location, the silicon composite electrode), a second piece of Kapton tape was placed on the copper foil. A hole was cut in the top Kapton layer that exposes 2–3 mm of copper around the diamond in order to contact the working electrode.

A PEEK compartment was screwed into the base with Kalrez O-rings to keep the electrochemical cell air-free. A copper mesh (100 mesh, 0.0045" wire diameter) loaded with the same silicon/carbon/binder composites used for the electrochemical experiments. Each mesh was cleaned by sonication in acetone and isoropropanol (15 min each) prior to casting. After cleaning,

the mesh was dipped in the aqueous slurry, excess slurry was wiped away, and the slurry was dried in a vacuum oven at 150 °C for 24 h. To prepare the electrochemical portion of the spectroelectrochemical experiment, the cell and mesh were brought into an Ar glovebox, leaving the cell under evacuation for 12 h to remove trace water. The mesh was added to the cell and 30 μL of electrolyte (7:3 ethylmethylcarbonate and ethylene carbonate, 1.2 M LiPF$_6$) was dropped onto the mesh. A 16 mm Celguard separator was then added an additional 20 μL was dropped onto the separator. Finally, a piece of Li foil was mechanically polished and added to the cell. Finally, a 0.5 mm spacer was added. The compartment was sealed using a second PEEK piece was a stainless-steel rod embedded to contact the spacer. A schematic of the assembled cell is shown in Figure S10. Afterwards, the fully constructed cell was brought out of the box and placed on the spectrometer. Two-electrode electrochemical cycling was performed by contacting the rod (counter and reference electrode) and copper foil (working electrode). The cell was held at open circuit at 9 h, subjected to 3 formation cycles at C/20, galvanostatically scanned to 0.1 V vs Li at C/5, and held at 0.1 V vs Li for 180 h. Throughout this experiment, infrared spectra were collected every 20 min.

Spectra were analyzed using Python 3.7.7. To remove detector drift during from spectra during the long experiments, a featureless region of the spectrum (2500 cm^{-1}) was used to benchmark the baseline position. A constant was subtracted from each spectrum to bring the absorbance at this position to zero. To plot ΔA, each spectrum was subtracted from the initial spectrum for each data set.

Author Contributions

T.R.M. helped conceive the project, developed the synthetic methods, interpreted the results, fabricated and tested electrochemical cells, analyzed all data, conducted mechanical measurements, and prepared figures. R.T.P. developed the in situ FTIR cells and techniques, collected spectroscopy data, and analyzed the spectroscopy data. J.E.C. developed the mechanical testing methods and interpreted the results. M.C.S. developed the voltage hold protocols and interpreted results. N.R.N. conceived the project, developed the in situ FTIR cells and techniques, and analyzed FTIR spectroscopy data. All authors contributed to the manuscript.

Conflicts of interest

There are no conflicts to declare.

Acknowledgements

References

1   A. Franco Gonzalez, N. H. Yang and R. S. Liu, *J. Phys. Chem. C*, 2017, **121**, 27775–27787.
2   J. K. Lee, C. Oh, N. Kim, J. Y. Hwang and Y. K. Sun, *J. Mater. Chem. A*, 2016, **4**, 5366–5384.
3   J. Hu, Y. Wang, D. Li and Y. T. Cheng, *J. Power Sources*, 2018, **397**, 223–230.
4   W. F. Ren, J. B. Le, J. T. Li, Y. Y. Hu, S. Y. Pan, L. Deng, Y. Zhou, L. Huang and S. G. Sun, *ACS Appl. Mater. Interfaces*, 2021, **13**, 639–649.
5   J. He and L. Zhang, *J. Alloys Compd.*, 2018, **763**, 228–240.
6   U. S. Vogl, P. K. Das, A. Z. Weber, M. Winter, R. Kostecki and S. F. Lux, *Langmuir*, 2014, **30**, 10299–10307.
7   J. Choi, K. Kim, J. Jeong, K. Y. Cho, M. H. Ryou and Y. M. Lee, *ACS Appl. Mater. Interfaces*, 2015, **7**, 14851–14858.
8   M. K. Burdette-Trofimov, B. L. Armstrong, A. M. Rogers, L. Heroux, M. Doucet, G. Yang, N. D. Phillip, M. K. Kidder and G. M. Veith, *J. Phys. Chem. C*, 2020, **124**, 13479–13494.
9   B. Hu, S. Jiang, I. A. Shkrob, J. Zhang, S. E. Trask, B. J. Polzin, A. Jansen, W. Chen, C. Liao, Z. Zhang and L. Zhang, *J. Power Sources*, 2019, **416**, 125–131.
10 W. Porcher, S. Chazelle, A. Boulineau, N. Mariage, J. P. Alper, T. Van Rompaey, J.-S. Bridel and C. Haon, *J. Electrochem. Soc.*, 2017, **164**, A3633–A3640.
11 B. Hu, I. A. Shkrob, S. Zhang, L. Zhang, J. Zhang, Y. Li, C. Liao, Z. Zhang, W. Lu and L. Zhang, *J. Power Sources*, 2018, **378**, 671–676.
12 K. A. Hays, B. Armstrong and G. M. Veith, *ChemElectroChem*, 2020, **7**, 3790–3797.
13 C. C. Nguyen, T. Yoon, D. M. Seo, P. Guduru and B. L. Lucht, *ACS Appl. Mater. Interfaces*, 2016, **8**, 12211–12220.
14 S. Jiang, B. Hu, Z. Shi, W. Chen, Z. Zhang and L. Zhang, *Adv. Funct. Mater.*, 2020, **30**, 1–9.
15 B. Hu, S. Jiang, I. A. Shkrob, S. Zhang, J. Zhang, Z. Zhang and L. Zhang, *ACS Appl. Energy Mater.*, 2019, **2**, 6348–6354.
16 P. F. Cao, G. Yang, B. Li, Y. Zhang, S. Zhao, S. Zhang, A. Erwin, Z. Zhang, A. P. Sokolov, J. Nanda and T. Saito, *ACS Energy Lett.*, 2019, **4**, 1171–1180.
17 Y. P. Chuang, Y. L. Lin, C. C. Wang and J. L. Hong, *ACS Appl. Energy Mater.*, 2021, **4**, 1583–1592.
18 S. Jiang, B. Hu, R. Sahore, H. Liu, G. F. Pach, G. M. Carroll, L. Zhang, B. Zhao, N. R. Neale and Z. Zhang, *ACS Appl. Energy Mater.*, 2019, **2**, 6176–6183.
19 C. Li, T. Shi, H. Yoshitake and H. Wang, *J. Mater. Chem. A*, 2016, **4**, 16982–16991.
20 K. A. Hays, R. E. Ruther, A. J. Kukay, P. Cao, T. Saito, D. L. Wood and J. Li, *J. Power Sources*, 2018, **384**, 136–144.
21 J. Bareño, I. A. Shkrob, J. A. Gilbert, M. Klett and D. P. Abraham, *J. Phys. Chem. C*, 2017, **121**, 20640–20649.

22 P. Parikh, M. Sina, A. Banerjee, X. Wang, M. S. D'Souza, J. M. Doux, E. A. Wu, O. Y. Trieu, Y. Gong, Q. Zhou, K. Snyder and Y. S. Meng, *Chem. Mater.*, 2019, **31**, 2535–2544.

23 R. T. Pekarek, A. Affolter, L. L. Baranowski, J. Coyle, T. Hou, E. Sivonxay, B. A. Smith, R. D. McAuliffe, K. A. Persson, B. Key, C. Apblett, G. M. Veith and N. R. Neale, *J. Mater. Chem. A*, 2020, **8**, 7897–7906.

24 Y. Ha, B. J. Tremolet De Villers, Z. Li, Y. Xu, P. Stradins, A. Zakutayev, A. Burrell and S. D. Han, *J. Phys. Chem. Lett.*, 2020, **11**, 286–291.

25 C. Stetson, Y. Yin, A. Norman, S. P. Harvey, M. Schnabel, C. Ban, C. S. Jiang, S. C. DeCaluwe and M. Al-Jassim, *J. Power Sources*, 2021, **482**, 228946.

26 S. D. Han, K. N. Wood, C. Stetson, A. G. Norman, M. T. Brumbach, J. Coyle, Y. Xu, S. P. Harvey, G. Teeter, A. Zakutayev and A. K. Burrell, *ACS Appl. Mater. Interfaces*, 2019, **11**, 46993–47002.

27 Y. Xu, K. Wood, J. Coyle, C. Engtrakul, G. Teeter, C. Stoldt, A. Burrell and A. Zakutayev, *J. Phys. Chem. C*, 2019, **123**, 13219–13224.

28 J. E. Coyle, M. T. Brumbach, G. M. Veith and C. A. Apblett, *J. Phys. Chem. C*, 2020, **124**, 8153–8161.

29 Y. J. Zhou, P. Luner and P. Caluwe, *J. Appl. Polym. Sci.*, 1995, **58**, 1523–1534.

30 K. Konca and P. Z. Çulfaz-Emecen, *J. Memb. Sci.*, 2019, **587**, 117175.

31 H. Hu, H. Xu, X. Dong, Q. Zhao, R. Wu, C. Meng, T. Cai and J. He, *Cellulose*, 2021, **28**, 5071–5085.

32 N. Bosco, S. Moffitt and L. T. Schelhas, *Prog. Photovoltaics Res. Appl.*, 2019, **27**, 340–345.

33 N. Bosco, J. Tracy and R. Dauskardt, *IEEE J. Photovoltaics*, 2019, **9**, 469–475.

34 Y. Park, S. Lee, S. S. Ha, B. Alunda, D. Y. Noh, Y. J. Lee, S. Kim and J. H. Seol, *Polymers*, 2019, **11**, 1–13.

35 D. Li, Y. Wang, J. Hu, B. Lu, D. Dang, J. Zhang and Y. T. Cheng, *J. Power Sources*, 2018, **387**, 9–15.

36 M. Schulze, M. Rodrigues, J. McBrayer, I. Bloom, A. Colclasure, G. Veith, D. Abraham, N. Neale, A. Burrell, J. Vaughey and C. Johnson, *Silicon Consortium Project Calendar Aging Electrochemical Screening Protocol 1.1.*, 2020.

37 M. Lewerenz, S. Käbitz, M. Knips, J. Münnix, J. Schmalstieg, A. Warnecke and D. U. Sauer, *J. Power Sources*, 2017, **353**, 144–151.

38 M. T. Ong, O. Verners, E. W. Draeger, A. C. T. Van Duin, V. Lordi and J. E. Pask, *J. Phys. Chem. B*, 2015, **119**, 1535–1545.

39 O. Borodin, M. Olguin, P. Ganesh, P. R. C. Kent, J. L. Allen and W. A. Henderson, *Phys. Chem. Chem. Phys.*, 2016, **18**, 164–175.

40 M. C. Schulze, G. M. Carroll, T. R. Martin, K. Sanchez-Rivera, F. Urias and N. R. Neale, *ACS Appl. Energy Mater.*, 2021, **4**, 1628–1636.

41 F. Shi, P. N. Ross, G. A. Somorjai and K. Komvopoulos, *J. Phys. Chem. C*, 2017, **121**, 14476–14483.